ACS OMEGA

Open Access

http://pubs.acs.org/journal/acsodf

Article

Efficient Removal of Diclofenac Sodium and Hg(II) on Graphene Oxide/UiO-66-$(OH)_2$ Composites

Tao Shen, Guodong Wu, Li Yin, Tianen Chen, JiYe Fan, Yuanhao Wang, and Shifeng Wang*

Cite This: *ACS Omega* 2025, 10, 17269−17279

Read Online

ACCESS | Metrics & More | Article Recommendations | Supporting Information

ABSTRACT: Developing efficient adsorbents for removal of organic pollutants and heavy metals is essential for environmental protection. In this study, a series of GO/UiO-66-$(OH)_2$ composites were synthesized and characterized using XRD, FT-IR, and SEM, confirming enhanced thermal stability, reduced aggregation, and maintained crystallinity of UiO-66-$(OH)_2$ due to GO incorporation. Batch adsorption experiments showed that GO increased the adsorption capacity, with GO-8/UiO-66-$(OH)_2$ achieving 324.2 mg/g for diclofenac sodium (DCF) and 429.3 mg/g for Hg^{2+}. DCF adsorption was primarily governed by physisorption, while Hg adsorption was chemisorptive, involving strong coordination with oxygen functional groups. Kinetic and isotherm studies revealed the suitability of the pseudo-second-order and Freundlich models, with thermodynamic analysis showing exothermic DCF adsorption and endothermic Hg^{2+} adsorption. The composites also exhibited high selectivity and stable regeneration, making them promising candidates for practical environmental remediation.

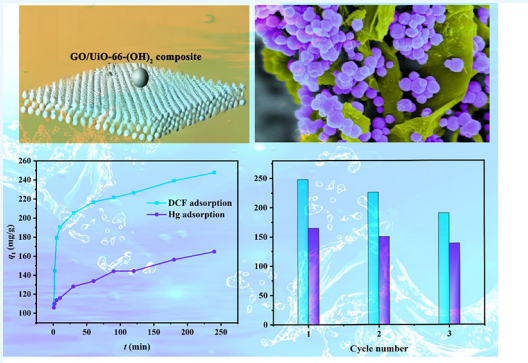

1. INTRODUCTION

The removal of metal ions and pharmaceutical contaminants from wastewater has become increasingly essential due to their significant environmental and public health impacts. Metal ions, such as lead, cadmium, mercury, and arsenic, are common pollutants in industrial wastewater and pose severe risks to aquatic ecosystems and human health due to their toxicity, persistence, and bioaccumulative nature.[1,2] Even at low concentrations, these metals can cause serious health problems including neurological disorders, kidney damage, and carcinogenic effects. Similarly, the presence of pharmaceuticals in wastewater has emerged as a growing concern. Pharmaceuticals, including antibiotics, hormones, and painkillers, are increasingly detected in water bodies due to improper disposal, excretion, and runoff from agricultural lands. These substances can potentially cause long-term health issues in humans through contaminated drinking water.[3] The persistence and complex chemical structures of pharmaceuticals make them challenging to remove using conventional treatment processes, thereby highlighting the need for more efficient and targeted removal strategies.[4]

Diclofenac sodium (DCF) is a widely used nonsteroidal anti-inflammatory drug (NSAID), which is frequently detected in aquatic environments due to its extensive applications in human and veterinary medicines.[5] Improper disposal, incomplete removal processes, and excretion result in the prevalence of DCF in water environments. DCF owns persistence and bioaccumulation potential, it can adversely affect the aquatic organisms by disrupting reproductive systems and leading to potential risks to human health.[6] Moreover, mercury ions (Hg^{2+}) are common in industrial wastewater, originating from industrial activities such as mining, chlor-alkali production, and battery manufacturing.[7] Hg^{2+} is highly toxic, persistent, and bioaccumulative, posing severe risks to ecosystems and human health. Even trace amounts of mercury can lead to neurological disorders, kidney damage, and carcinogenic effects.[8] Its removal is crucial to mitigate its widespread environmental and health hazards. Therefore, removal of DCF and Hg^{2+} from wastewater is important in both wastewater treatment and environmental protection.

The development of porous adsorbents, such as metal−organic frameworks (MOFs) and graphene-based composites, offers promising solutions for addressing these challenges. These materials can effectively capture and remove metal ions and pharmaceuticals from wastewater, thus reducing their environmental impact and safeguarding public health.[9,10] The ongoing research in this field aims to optimize the adsorption properties of these materials, improve their regeneration and recyclability, and ensure their practical applicability in large-scale wastewater treatment processes. The incorporation of

Received: October 17, 2024
Revised: December 16, 2024
Accepted: January 6, 2025
Published: April 24, 2025

https://doi.org/10.1021/acsomega.4c09459
ACS Omega 2025, 10, 17269−17279

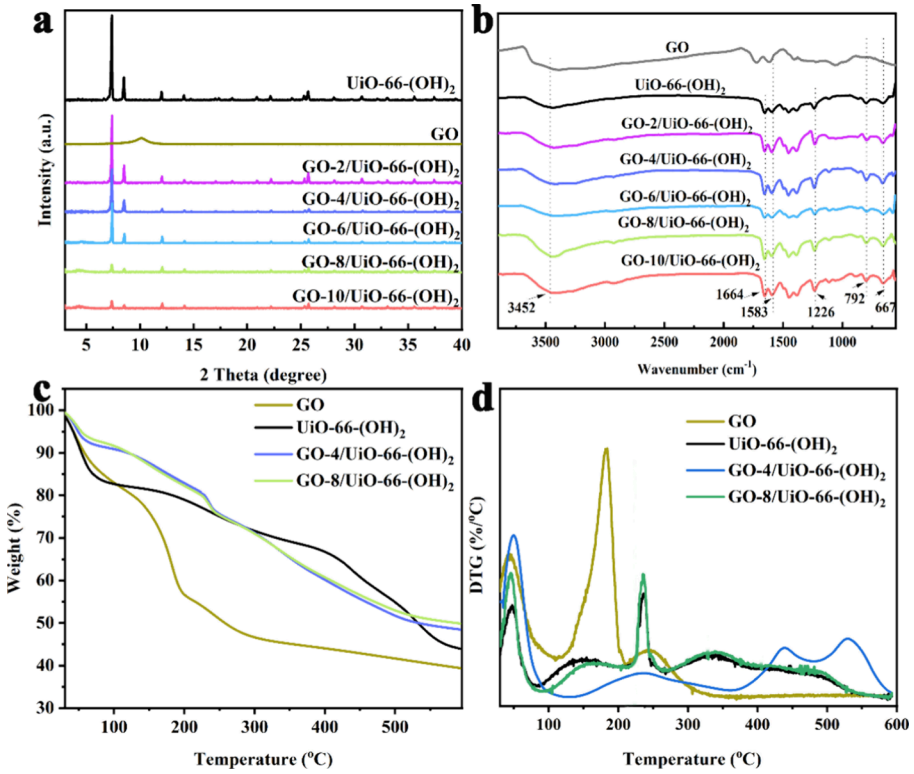

Figure 1. XRD pattern (a), FT-IR spectra (b), TG (c), and DTG (d) curves of GO, UiO-66-$(OH)_2$, and GO/UiO-66-$(OH)_2$ composites.

UiO-66 with graphene oxide (GO) to form composite materials has garnered significant attention in the field of environmental remediation.[11] UiO-66 is known for its exceptional chemical stability, high surface area, and tunable pore size, making it an ideal candidate for the adsorption of various pollutants in water.[12] However, the relatively low electrical conductivity and potential agglomeration of MOF particles can limit their practical applications. To address these challenges, GO is introduced as a dopant due to its excellent mechanical properties, high surface area, and outstanding electrical conductivity. The synergy between UiO-66 and GO in the composite material enhances the adsorption capacity, stability, and reusability, offering a promising solution for the efficient removal of organic and inorganic pollutants from water. This research aims to explore the mechanisms behind the enhanced adsorption performance of UiO-66/GO composites, focusing on their potential applications in wastewater treatment.[13]

Recent studies have demonstrated the remarkable performance of UiO-66/GO composites in removing a wide range of contaminants from aqueous solutions. Research has shown that the presence of GO not only improves the dispersion of UiO-66 particles but also provides additional adsorption sites, leading to increased pollutant uptake.[14,15] Furthermore, advancements in synthesis techniques have allowed for better control over the morphology and structure of the composites, resulting in improved adsorption efficiency and recyclability. Current research is focusing on optimizing the synthesis methods, understanding the adsorption mechanisms at the molecular level, and exploring the scalability of these composites for real-world wastewater treatment applications. This progress underscores the potential of UiO-66/GO composites as a highly effective and sustainable solution for water purification.

Herein, a series of GO/UiO-66-$(OH)_2$ composites were synthesized to serve as efficient adsorbents for the simultaneous removal of DCF and Hg^{2+} from aqueous solution. A combination of structural characterization and batch experiments was carried out. Adsorption mechanisms were discussed by characterizing the fresh and spent adsorbents, discussing influence factors, calculating adsorption kinetics, isotherms, and also thermodynamics. The advancement and unique conclusion in this study reveals in the exploration of simultaneous removal of multiple pollutants the mechanistic insights as well as the real-environment applicability. The results provide valuable insights into the dual-functional capability, enhanced adsorption efficiency, and practical applicability, which are crucial for scaling up and implementing these composites in industrial wastewater treatment.

2. EXPERIMENTAL SECTION

2.1. Materials. All chemicals including zirconium chloride ($ZrCl_4$, 99.9%), *N*,*N*-dimethylformamide (DMF, C_3H_7NO, 98%), methanic acid (analytic grade, HCOOH, 99%), and 2,5-dihydroxyterephthalic acid (H_2DHTP, 98%) were supplied by Shanghai Aladdin Biochemical Technology Co., Ltd. without further purification. Diclofenac sodium (DCF) and mercuric nitrate solution ($HgNO_3$, 1 g/L) were obtained from Sigma-Aldrich. Graphene oxide (GO) was offered by Nanjing XFNANO Materials Tech Co., Ltd.

2.2. Synthesis of GO/UiO-66-$(OH)_2$ Composites. UiO-66-$(OH)_2$ was synthesized by dissolving certain amounts of $ZrCl_4$ (1.25 g) in 50 mL of DMF and 10 mL of HCl under ultrasound for 20 min. After adding H_2DHTP (1.47 g) and 100 mL of DMF to the solution, the mixture was placed under 120 °C for 24 h. GO/UiO-66-$(OH)_2$ composites were synthesized by one-pot hydrothermal methods under the same conditions of UiO-66-$(OH)_2$ and different amounts of

https://doi.org/10.1021/acsomega.4c09459
ACS Omega 2025, 10, 17269−17279

GO (20, 40, 60, 80, and 100 mg) into the $ZrCl_4$ solution to obtain the final resultants, which were denoted as GO-2/UiO-66-$(OH)_2$, GO-4/UiO-66-$(OH)_2$, GO-6/UiO-66-$(OH)_2$, GO-8/UiO-66-$(OH)_2$ and GO-10/UiO-66-$(OH)_2$, respectively.

2.3. Adsorption and Regeneration Tests. The adsorption performances of the GO, UiO-66-$(OH)_2$, and GO/UiO-66-$(OH)_2$ composites toward DCF and Hg^{2+} were tested by batch experiments. During the test, 0.03 g of the adsorbent (GO, UiO-66-$(OH)_2$, or GO/UiO-66-$(OH)_2$) were dispersed into 30 mL of the pollutant solution (DCF and Hg^{2+}) under 25 °C for 3 h. In the ratio optimization process, the initial concentrations of DCF and Hg^{2+} were 300 and 200 mg/L, respectively (T = 25 °C, t = 3 h to ensure the adsorption equilibrium). In the test of time effects, the adsorption time were selected as 1, 2, 5, 10, 30, 60, 90, 120, 180, and 240 min (T = 25 °C, the initial concentrations of DCF and Hg^{2+} were 300 and 200 mg/L), respectively. In the tests of adsorption temperature and adsorbate concentration, the temperature (25, 40, and 55 °C) and initial concentrations of DCF and Hg^{2+} (200, 250, 300, 350, 400, 500, and 600 mg/L) were adopted. In the tests of pH effects, the solution pH was adjusted to 4, 5, 6, 7, 8, and 9. In the DCF and Hg^{2+} binary component systems, the experimental conditions were the same as the ratio optimization process. After absorbing, the used adsorbents were collated, and 50 mg of the spent absorbent was dispersed in 0.1 mL of HCl solution (50 mL). After immersing under 25 °C for 6 h, the samples were centrifuged and dried under 60 °C for 24 h. The readsorption conditions were the same as the ratio optimization process. After adsorption, the sample was centrifuged, and the absorbance of supernatant was monitored by a UV−vis spectrophotometer to ensure the DCF concentration. The concentration of Hg^{2+} was tested by inductively coupled plasma mass spectrometry (ICP-MS). The adsorption capacity of the adsorbent could be calculated by the following equation:

$$q_e = \frac{C_0 - C_e}{m} V \quad (1)$$

where q_e is the adsorption capacity (mg/g), C_0 and C_e are the initial and equilibrium DCF/Hg^{2+}concentrations (mg/L), respectively, m represents the mass of adsorbent (g), and V stands for the volume of solution (mL). All of the adsorption experiments were carried out twice to ensure the data reliability.

Details of Characterization, the equations of adsorption kinetics, isotherms, and thermodynamics were listed in the Supporting Information.

3. RESULTS AND DISCUSSION

3.1. Characterization. The XRD patterns of GO, UiO-66-$(OH)_2$, and GO/UiO-66-$(OH)_2$ composites are shown in Figure 1a. The sharp peaks indicate a well-crystallized structure, which is characteristic of the UiO-66-type MOF. The intense peak at around 7° suggests a highly ordered crystalline phase.[16] In the case of GO, the broad peak centered around 10° is typical for GO, indicating its layered structure with some degree of disorder due to oxygen-containing functional groups.[17] In the XRD pattern of GO/UiO-66-$(OH)_2$ composites, the peaks corresponding to UiO-66-$(OH)_2$ are still visible, but with reduced intensity as the GO content increases, which may be due to the effects of GO on the crystallinity of UiO-66-$(OH)_2$. Great crystallinity of UiO-66-$(OH)_2$ is maintained in GO-6/UiO-66-$(OH)_2$. Notably, although the characteristic peak of GO is inconspicuous in the pristine GO/UiO-66-$(OH)_2$ composites, it appears after the composite is ground to break the UiO-66-$(OH)_2$ crystallinity, verifying the successful synthesis of GO/UiO-66-$(OH)_2$ composites.

The FT-IR spectra of the pristine GO, UiO-66-$(OH)_2$, and GO/UiO-66-$(OH)_2$ composites are shown in Figure 1b. The characteristic peaks of GO emerge at 3452 cm^{-1}, 1740 cm^{-1}, and 1636 cm^{-1}, indicating the strong hydrophilicity and abundant oxygen-containing functional groups on the GO surface, which can further serve as nucleation sites for binding MOF particles and regulate the morphology of the resultant composites.[18] As indicated by the strength variation of the peaks at 3452 cm^{-1} (induced by the adsorbed H_2O) and 667 cm^{-1} (induced by the vibration of structural −OH), the hydrophilicity of GO/UiO-66 composites is stronger with the relative ratio of GO to UiO-66 increasing,[19,20] indicating the stronger hydrophilicity of pristine GO than UiO-66-$(OH)_2$. Peaks at 1664 $cm^{-1}$and 1583 cm^{-1} are derived from −COOH, whereas the peak at 792 cm^{-1} resulted from C−H.[21] C−O−Zr gave rise to the peak at 1226 cm^{-1}, indicating that the addition of GO had little influence on the structure of UiO-66-$(OH)_2$.[22]

TG curves of GO, UiO-66-$(OH)_2$, GO-4/UiO-66-$(OH)_2$, and GO-8/UiO-66-$(OH)_2$ are depicted in Figure 1c. Main weight loss stages in GO occurs between 100 °C and 400 °C, whereas the decomposition of UiO-66-$(OH)_2$ happened in the temperature range of 0−100 °C and 100−400 °C.[23,24] In the composite materials, improved thermal stability and hydrophobicity of GO-4/UiO-66-$(OH)_2$ and GO-8/UiO-66-$(OH)_2$ are obtained, verifying the existence of strong interactions between GO and UiO-66-$(OH)_2$. Notably, similar weight losses are observed for GO-4/UiO-66-$(OH)_2$ and GO-8/UiO-66-$(OH)_2$ (Figure 1d). The UiO-66-$(OH)_2$ in both GO-4/UiO-66-$(OH)_2$ and GO-8/UiO-66-$(OH)_2$ provides a stabilizing matrix that delays the thermal decomposition of GO, resulting in similar overall thermal behavior despite the slight variation in UiO-66-$(OH)_2$ content.

In the DTG curves, GO exhibits pronounced peaks below 250 °C, reflecting the rapid decomposition of functional groups, while UiO-66-$(OH)_2$ shows a more gradual decomposition profile, confirming its superior thermal resistance. The GO-UiO-66-$(OH)_2$ composites show reduced peak intensity compared with GO, highlighting their enhanced thermal stability. This improvement is likely due to the synergistic interaction between the GO layers and the UiO-66-$(OH)_2$ framework, which mitigates the rapid degradation of GO and contributes to a greater structural integrity.

To clarify the effects of GO on the morphology of UiO-66-$(OH)_2$, the SEM images of GO, UiO-66-$(OH)_2$, and GO-4/UiO-66-$(OH)_2$ and GO-8/UiO-66-$(OH)_2$ are shown in Figure 2. GO appears as thin, crumpled sheets or layers. The lamellar structure is clearly visible with wrinkles and folds, characteristic of the high surface area and layered arrangement. UiO-66-$(OH)_2$ exhibits a well-defined particle structure with a rough, porous surface, the particles appear agglomerated, forming a relatively dense cluster with microscale size. After combining with GO, UiO-66-$(OH)_2$ particles were distributed across the GO sheets. The spherical MOF particles are well-deposited onto the GO surface, but the GO structure is still visible underneath. The relatively uniform distribution of MOF particles suggests a moderate loading of UiO-66-$(OH)_2$, leading to a balanced interaction between the MOF and GO. Compared with GO-8/UiO-66-$(OH)_2$, GO-4/UiO-66-$(OH)_2$

https://doi.org/10.1021/acsomega.4c09459
ACS Omega 2025, 10, 17269−17279

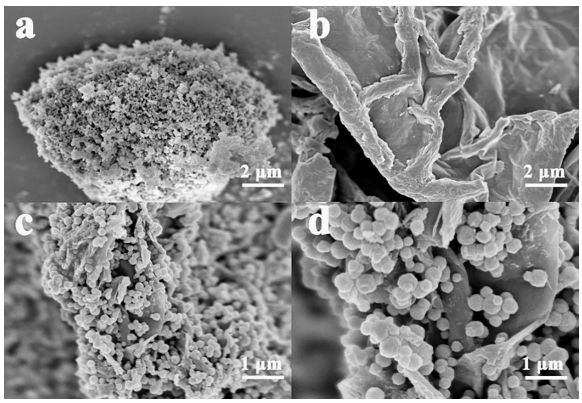

Figure 2. SEM image of UiO-66-$(OH)_2$ (a), GO (b), GO-4/UiO-66-$(OH)_2$ (c), and GO-8/UiO-66-$(OH)_2$ (d).

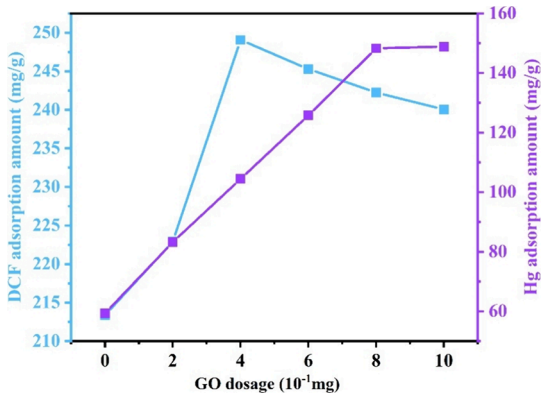

Figure 3. Effect of GO dosage on the adsorption of DCF and Hg^{2+}.

exhibits a noticeable increase in the amount of UiO-66-$(OH)_2$ particles, and the more densely packed particles and higher coverage ratio on the GO surface demonstrates stronger interactions between GO and UiO-66-$(OH)_2$. The structural properties of UiO-66-$(OH)_2$, GO-4/UiO-66-$(OH)_2$, and GO-8/UiO-66-$(OH)_2$ are further measured and presented in Figure S1. The surface areas of UiO-66-$(OH)_2$, GO-4/UiO-66-$(OH)_2$, and GO-8/UiO-66-$(OH)_2$ are 1102.04, 1056.65, and 710.47 m^2/g, and the corresponding pore sizes decrease from 0.68 to 0.61 and 0.58 nm, respectively. The BET results show that the surface area and pore volume decrease progressively from UiO-66-$(OH)_2$ to GO-4/UiO-66-$(OH)_2$ and GO-8/UiO-66-$(OH)_2$, and this trend is primarily due to the increasing coverage of UiO-66-$(OH)_2$ particles by GO sheets. Excessive GO loading (GO-8/UiO-66-$(OH)_2$) leads to particle aggregation and overlapping, which physically blocks pores and limits the accessibility of adsorption sites, thereby significantly reducing the overall surface area and porosity, consistent with SEM results.

Compared with the pristine GO and UiO-66-$(OH)_2$, the morphology variation of the composites may be due to the following reason: (i) Functional group interactions. The abundant oxygen-containing functional groups on the GO surface can interact with the hydroxyl groups (−OH) in the organic ligand of UiO-66-$(OH)_2$, which would disrupt the crystallization process of UiO-66-$(OH)_2$.[25] (ii) Nucleation and growth process. GO serves as the heterogeneous nucleation site, which can change the nucleation and crystal growth dynamics, leading to the altered MOF particle shape, size or hierarchical structures.[26] (iii) Layered structure of GO. GO is characterized by a two-dimensional layered structure, which can impose spatial constraints during the composite process. The formation of a composite with altered particle morphology may physically prevent the agglomeration of MOF particles, promoting the formation of smaller and more dispersed structures. These morphological variations may change the surface character and porosity of the resultant composites, contributing to better adsorption performance in wastewater treatment processes.

3.2. Adsorption Test. *3.2.1. Effect of GO Dosage.* The effect of GO dosage on the adsorption processes toward DCF and Hg is shown in Figure 3. The adsorption capacity of the raw UiO-66-$(OH)_2$ toward DCF and Hg^{2+} are 213.4 and 59.4 mg/g. The adsorption capacities of pristine GO toward DCF and Hg^{2+} are 150.4 and 188.2 mg/g (the initial concentrations of DCF and Hg^{2+} were 300 and 200 mg/L, respectively). The functional groups on the GO surface can provide $\pi-\pi$ interactions or hydrogen bonding toward DCF and provide complexation or electrostatic interactions toward Hg^{2+}. This adsorption capacity of pristine GO highlights its essential role in complementing the adsorption efficiency of UiO-66-$(OH)_2$, ensuring a synergistic effect on the removal of both organic and inorganic pollutants. Compared with UiO-66-$(OH)_2$, GO has relatively lower adsorption capacity toward DCF and higher adsorption capacity toward Hg^{2+}. When incorporated into the composite with UiO-66-$(OH)_2$, GO contributes to improving the dispersion of UiO-66-$(OH)_2$, reducing agglomeration and increasing the accessibility of active sites. While the exact contribution of GO in the composite depends on the synthesis ratio and material structure, its high intrinsic adsorption capacity suggests that it plays a significant role in pollutant removal.

Adulteration of GO into UiO-66-$(OH)_2$ contributes to enhanced adsorption processes toward both DCF and Hg^{2+}. For DCF uptake, the absorptivity presents a sharp increase and is followed by a gradual decrement with increasing GO dosage, which may be due to the morphology regulation of GO on the UiO-66-$(OH)_2$ particles. In comparison, great affinity of GO toward Hg contributed continuously increased Hg uptake with the GO dosage. Therefore, the enhancement of GO on adsorption processes mainly functioned in two ways: (i) The regulation of MOF morphology and relieve of MOF aggregation. (ii) The introduction of addition adsorption sites into the MOF. The highest adsorption capacity reached 249.1 mg/g (GO-8/UiO-66-$(OH)_2$ for DCF uptake) and 148.8 mg/g (GO-10/UiO-66-$(OH)_2$ for Hg^{2+} uptake), respectively. Taking both the adsorption capacity and the cost-effectiveness concepts into consideration, GO-8/UiO-66-$(OH)_2$ was selected as the most optimized dosage. The adsorption amounts of DCF and Hg^{2+} on GO-8/UiO-66-$(OH)_2$ were 242.2 and 148.3 mg/g, respectively.

3.2.2. Effect of Time and Adsorption Kinetics. The effect of time and adsorption kinetics are listed in Figure 4 and Table 1. The adsorption behavior of DCF and Hg^{2+} by GO-8/UiO-66-$(OH)_2$ follows distinct kinetic profiles over time. In the case of DCF adsorption, the adsorption capacity exhibits a rapid increase during the initial phase, rising sharply from 109.4 to 216.8 mg/g within 60 min, indicating the strong affinity of GO-8/UiO-66-$(OH)_2$ toward DCF. Following this initial phase, the rate of adsorption gradually decelerates, with the adsorption capacity reaching around 247.7 mg/g at 240 min.

As shown in Figure 4, the adsorption of GO-8/UiO-66-$(OH)_2$ toward Hg^{2+} proceeds at a noticeably slower rate. The

https://doi.org/10.1021/acsomega.4c09459
ACS Omega 2025, 10, 17269−17279

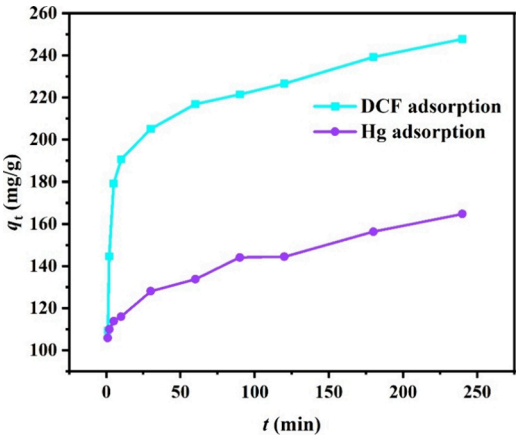

Figure 4. Effect of time on the adsorption of DCF and Hg^{2+} on GO-8/UiO-66-$(OH)_2$.

Table 1. Kinetic Parameters for the Adsorption of DCF/Hg on GO-8/UiO-66-$(OH)_2$

		adsorbates	
kinetic model	parameter	DCF	Hg
	$q_{e,exp}$	247.7	164.7
pseudo-first-order	$q_{e,cal}$	107.8	72.2
	k_1 (10^{-2})	1.95	1.74
	R^2	0.8549	0.8122
pseudo-second-order	$q_{e,cal}$	245.7	162.3
	k_2 (10^{-2})	0.09	0.11
	R^2	0.9974	0.9942
intraparticle diffusion	k_{id}	4.14	3.92
	C (10^2)	1.83	1.05
	R^2	0.9451	0.8834

adsorption capacity increases linearly over time, from 105.8 to 164.7 mg/g. This suggests that the active adsorption sites for Hg have not yet been fully occupied. Disparity in adsorption kinetics and capacity could be attributed to the selective affinity for DCF and Hg^{2+} as well as the differing physicochemical properties of the two adsorbates.

Based on the kinetic fitting results provided for the adsorption of DCF and Hg^{2+} onto GO-8/UiO-66-$(OH)_2$, the adsorption processes of these two adsorbates exhibit significant differences in both adsorption rate and capacity.[27]

The experimental adsorption capacity of DCF is 247.7 mg/g, which is substantially higher than that of Hg^{2+} (164.7 mg/g), suggesting that GO-8/UiO-66-$(OH)_2$ has a much higher affinity for DCF than Hg^{2+}. When comparing the kinetic models, the pseudo-first-order model results show a lower calculated adsorption capacity for both DCF (107.8 mg/g) and Hg^{2+} (72.2 mg/g), indicating a relatively poor fit,[21,22] as reflected by the lower R^2 values (0.8549 and 0.8122 for DCF and Hg^{2+}, respectively). The pseudo-second-order model provides a much better fit for both DCF and Hg^{2+} adsorption, with calculated adsorption capacities closely matching the experimental values. The R^2 values are notably higher (0.9974 for DCF and 0.9942 for Hg^{2+} adsorption, respectively), indicating that the adsorption processes are more accurately described by the pseudo-second-order kinetic model, which implies that chemisorption is likely the rate-limiting step in the adsorption process.[28−30] The intraparticle diffusion model shows that the diffusion rate constants are comparable for both DCF (4.14) and Hg^{2+} (3.92), suggesting that intraparticle diffusion contributes similarly to the overall adsorption process for both adsorbates.[31] However, the higher R^2 value for DCF (0.9451) compared to Hg^{2+} (0.8834) further supports that DCF adsorption reaches equilibrium more rapidly and fits the intraparticle diffusion model better.

In conclusion, the adsorption of DCF is faster and reaches a higher capacity than that of Hg^{2+} on GO-6/UiO-66-$(OH)_2$. The Pseudo-second-order model provides the best fit for both adsorbates, suggesting that chemisorption governs the overall adsorption mechanism, while intraparticle diffusion plays a secondary role in the adsorption dynamics.

3.2.3. Effect of Concentration and Adsorption Isotherms. The adsorption of DCF onto GO-8/UiO-66-$(OH)_2$ increases with rising initial concentrations across all temperatures, as shown in Figure 5. At 25 °C (Figure 5a), the adsorption capacity increases from 194.3 at 200 mg/L to 275.8 at 600 mg/L. A similar trend is observed at 40 and 55 °C, though the maximum adsorption capacities are lower, reaching about 291.9 mg/g and 361.6 mg/g at 600 mg/L, respectively. This indicates that higher DCF concentrations enhance the mass transfer driving force and the availability of active sites, leading to increased adsorption.

The adsorption of Hg onto GO-8/UiO-66-$(OH)_2$ increases significantly with rising initial concentrations across all temperatures (Figure 5b). At 25 °C, Hg uptake increases from 148.3 mg/g at 200 mg/L to 331.9 mg/g at 600 mg/L.

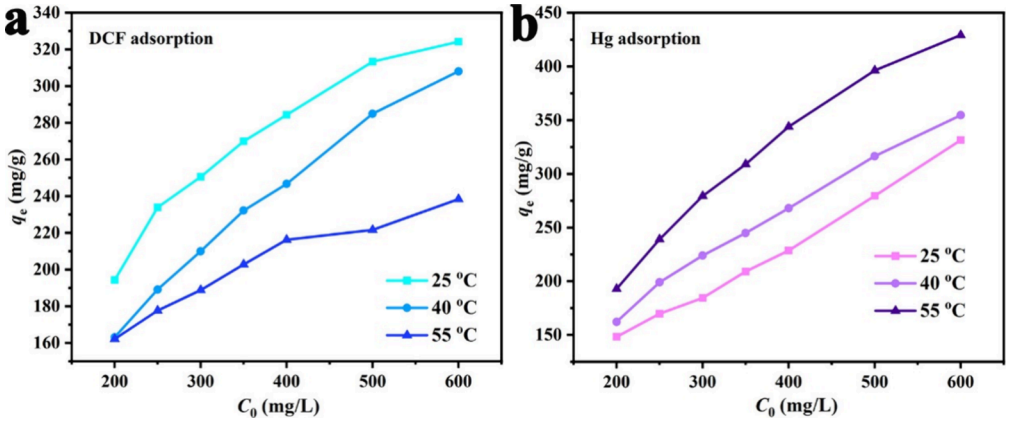

Figure 5. Effect of concentration and temperature on the adsorption of DCF (a) and Hg^{2+} (b) on GO-8/UiO-66-$(OH)_2$.

https://doi.org/10.1021/acsomega.4c09459
ACS Omega 2025, 10, 17269−17279

Table 2. Adsorption Isotherm Constants for the Adsorption of DCF/Hg on GO-8/UiO-66-$(OH)_2$

		adsorbates					
		DCF			Hg		
		298 K	313 K	328 K	298 K	313 K	328 K
Langmuir	q_{max}	300.0	245.93	240.32	506.02	433.76	423.95
	K_L	0.264	0.020	0.045	0.006	0.014	0.10
	R^2	0.7518	0.9953	0.8682	0.8633	0.9488	0.9193
Freundlich	K_f (10^2)	1.56	0.52	0.85	0.15	0.39	1.34
	n	7.76	3.18	5.79	1.84	2.51	4.34
	R^2	0.9950	0.9951	0.9774	0.9830	0.9985	0.9829

Similarly, at 40 and 55 °C, the adsorption capacity follows the same trend, but with higher values. At 40 °C, the adsorption capacity rises from 162.2 to 354.6 mg/g, while at 55 °C, it increases from 200.0 mg/g to a maximum of 429.3 mg/g at 600 mg/L. These results indicate that higher initial concentrations enhance the mass transfer driving force, enabling more Hg^{2+} to interact with the available adsorption sites.[32]

For DCF adsorption (Table 2), the Langmuir constant follows a decreasing trend with temperature, dropping from 0.264 L/mg at 298 K to 0.045 L/mg at 328 K, indicating that the affinity of the adsorbent for DCF weakens at higher temperatures. The Freundlich constant shows a similar pattern, decreasing from 1.56 (10^2) mg/g at 298 K to 0.85 (10^2) mg/g at 328 K, further supporting the conclusion that the adsorption of DCF is more favorable at lower temperatures. The n values, which range from 7.76 to 5.79, suggest that DCF adsorption onto GO-8/UiO-66-$(OH)_2$ is a favorable process, especially at lower temperatures.

For Hg^{2+} adsorption, the Langmuir constant increases with temperature, from 0.006 L/mg at 298 K to 0.10 L/mg at 328 K, indicating that the affinity between Hg^{2+} and the adsorbent improves with increasing temperature.[33] The Freundlich constant increases significantly with temperature, from 0.15 (10^2) mg/g at 298 K to 1.34 (10^2) mg/g at 328 K, while the n values indicate a shift from less favorable adsorption at lower temperatures (1.84 at 298 K) to more favorable adsorption at higher temperatures (4.34 at 328 K). This suggests that the adsorption of Hg^{2+} is endothermic, with stronger interactions occurring at higher temperatures.[34]

3.2.4. Effect of Temperature and Adsorption Thermodynamics. During the exploration stage of the temperature effects, 25 °C, 40 °C, and 55 °C are chosen based on the following reasons: (i) Temperature range: the temperature of 25 °C represents the room temperature. 40 °C is related to the conditions in industrial applications, whereas the temperature of 55 °C is relevant to thermal water treatment processes. (ii) Thermodynamic analysis: the selected temperatures can help to calculate the thermodynamic parameters. (iii) Data comparability: The broad temperature range between 25 °C and 55 °C ensures sufficient variation in adsorption capacity to obtain reliable data. (iv) Adsorption mechanism: The temperature can influence the adsorption mechanism. Lower temperatures (such as 25 °C) favor a physical adsorption process while higher temperatures may promote chemical adsorption.[35−37] The selected temperatures between 25 and 55 °C can fully cover the transition process, helping to identify the adsorption nature and the dependence on temperature.

Temperature has an inverse effect on adsorption capacity, with the highest values observed at 25 °C. As the temperature rises to 40 °C and 55 °C, the adsorption capacity declines, suggesting an exothermic adsorption process. This decrease in adsorption with increasing temperature indicates that physisorption is likely the dominant mechanism, where higher temperatures weaken the adsorbate−adsorbent interactions, reducing the adsorption efficiency. The adsorption capacity also shows a positive correlation with the temperature, indicating an endothermic adsorption process. At 55 °C, the maximum adsorption capacity of 400 mg/g at 600 mg/L is significantly higher than the 350 mg/g observed at 40 °C and the 300 mg/g at 25 °C. This temperature dependence suggests that chemisorption plays a major role in Hg^{2+} adsorption as higher temperatures likely promote stronger interactions between Hg^{2+} and the adsorbent surface. Therefore, the increased adsorption with temperature and concentration points toward a mechanism where chemisorption is the dominant process, with stronger binding interactions occurring at elevated temperatures. The adsorption of DCF onto GO-8/UiO-66-$(OH)_2$ is exothermic and more favorable at lower temperatures, while the adsorption of Hg^{2+} is endothermic and benefits from higher temperatures. These trends are supported by both Langmuir and Freundlich isotherm parameters, highlighting the distinct thermodynamic behavior of the two adsorbates.

The thermodynamic analysis reveals distinct differences between the adsorption behaviors of DCF and Hg^{2+} onto GO-8/UiO-66-$(OH)_2$. For DCF, the value of ΔG^θ becomes increasingly positive with rising temperature, from 3.29 kJ/mol at 298 K to 10.18 kJ/mol at 328 K (Table 3), indicating that the adsorption becomes less spontaneous at higher temperatures.[38] This is further supported by the negative entropy change ΔS^θ of −181.05 J/(mol·K), reflecting a more ordered structure of DCF on the adsorbent surface. The negative enthalpy change ΔH^θ of −49.36 kJ/mol confirms that the adsorption process is exothermic, which aligns with the observed decrease in adsorption capacity as the temperature increases. These data suggest that DCF adsorption is primarily driven by physical interactions, which are less favorable at elevated temperatures.[39]

Table 3. Thermodynamic Parameters for the Adsorption of DCF/Hg on GO-8/UiO-66-$(OH)_2$

	ΔG^θkJ/mol				
adsorbate	T = 298 K	T = 313 K	T = 328 K	ΔS^θ J/(mol·K)	ΔH^θ kJ/mol
DCF	3.29	8.46	10.18	−181.05	−49.36
Hg	12.68	11.11	6.28	209.73	75.67

In contrast, the adsorption of Hg^{2+} demonstrates an endothermic nature, as evidenced by the positive enthalpy change ΔH^θ of 75.67 kJ/mol. The value of ΔG^θ becomes less

https://doi.org/10.1021/acsomega.4c09459
ACS Omega 2025, 10, 17269−17279

positive with rising temperature, decreasing from 12.68 at 298 K to 6.28 at 328 K, indicating that the adsorption becomes more spontaneous as the temperature increases. The positive entropy change ΔS^{θ} of 209.73 J/(mol·K) suggests an increase in disorder at the solid−liquid interface potentially due to the release of water molecules or other ligands during Hg adsorption. These thermodynamic parameters highlight that the adsorption of Hg^{2+} is endothermic and favored at higher temperatures, in contrast to the exothermic, less favorable adsorption of DCF at elevated temperatures.

3.2.5. Effect of pH. The effect of pH on the adsorption capacities of DCF and Hg^{2+} by GO-8/UiO-66-$(OH)_2$ is shown in Figure 6. For DCF, the adsorption capacity decreases

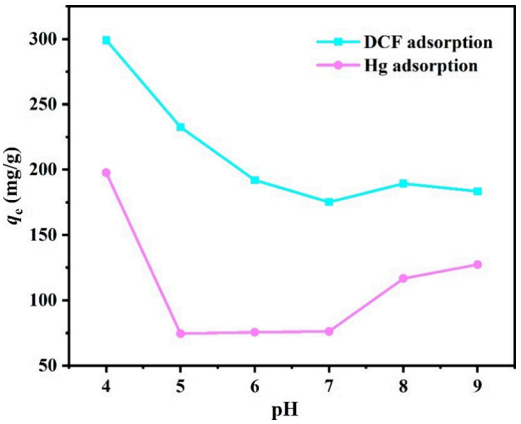

Figure 6. Effect of pH on the adsorption of DCF and Hg^{2+} on GO-8/UiO-66-$(OH)_2$.

sharply from 299.1 mg/g at pH 4 to 191.9 mg/g at pH 6 followed by a gradual decline and stabilization between pH 6 and pH 9. DCF is an amphoteric molecule, and its speciation depends on the solution pH. The pK_a values of DCF (typically around 4.2 and 9.5) govern its protonation and deprotonation states. At pH < 4.2, DCF exists predominantly in its neutral form, which has weaker interactions with the adsorbent due to reduced electrostatic interactions. At pH 4.2−9.5, DCF exists primarily in its deprotonated (anionic) form.[40] The negatively charged DCF molecules interact strongly with positively charged sites on the adsorbent surface, resulting in a higher adsorption. At pH > 9.5, both DCF and the adsorbent surface become negatively charged due to deprotonation, leading to electrostatic repulsion and reduced adsorption.[41] The values of zeta potential are measured under different solution pH. The zeta potential of GO-8/UiO-66-$(OH)_2$ are −4.5, −9.0, −15.4, −22.7, −25.4, and −28.4 eV, corresponding to the solution pH of 4, 5, 6, 7, 8, and 9, respectively. The adsorbent surface becomes increasingly negatively charged, which reduces the electrostatic attraction to anionic DCF molecules. Additionally, competition from hydroxide ions (OH^-) further decreases DCF adsorption at higher pH.

In contrast, the adsorption of Hg^{2+} exhibits a different trend, with the adsorption capacity decreasing from 197.6 mg/g at pH 4 to a minimum around pH 6 and then increasing slightly at higher pH values. The decrease in the level of adsorption at lower pH values can be attributed to competition between H^+ and Hg^{2+} for the available adsorption sites. At low pH (e.g., pH 4), the dominant species of mercury in solution is free Hg^{2+} ions, which are highly reactive and readily adsorbed onto the functional groups of the adsorbent. At higher pH values (e.g., pH 8 or 9), Hg^{2+} ions tend to hydrolyze and form neutral or negatively charged species, such as $Hg(OH)_2$ or $Hg(OH)_3^-$.[42] These species have weaker interactions with the adsorbent, resulting in lower adsorption at higher pH. At pH 4, some adsorption sites on the composite remain deprotonated, allowing Hg^{2+} ions to adsorb effectively despite the presence of H^+ ions.[43] The interaction between Hg^{2+} and the functional groups (e.g., carboxyl and hydroxyl groups on GO and UiO-66-$(OH)_2$) may outweigh the competition from the H^+ ions under these conditions. Conversely, at pH 8 or 9, the surface charge of the adsorbent becomes increasingly negative due to deprotonation, which could reduce the electrostatic attraction toward neutral or negatively charged Hg species. This behavior suggests that the adsorption of Hg^{2+} is driven by both surface complexation and electrostatic interactions, which are pH-dependent.

3.2.6. Applicability Tests under a Real Environment. To explore the applicability of GO-8/UiO-66-$(OH)_2$ under a real environment, the regenerability and selectivity of GO-8/UiO-66-$(OH)_2$ toward Hg^{2+} are tested. Benefited from the stability of GO and UiO-66-$(OH)_2$ components, acid pickling of GO-8/UiO-66-$(OH)_2$ after three cycles, the adsorption capacity of GO-8/UiO-66-$(OH)_2$ toward DCF (Hg^{2+}) decreased from 247.7 (164.7 mg/g) to 225.8 (150.3 mg/g) and 190.4 (138.7 mg/g), respectively (shown in Figure 7a). The observed differences in regeneration performance can be attributed to the adsorption mechanisms: DCF likely involves weaker, more

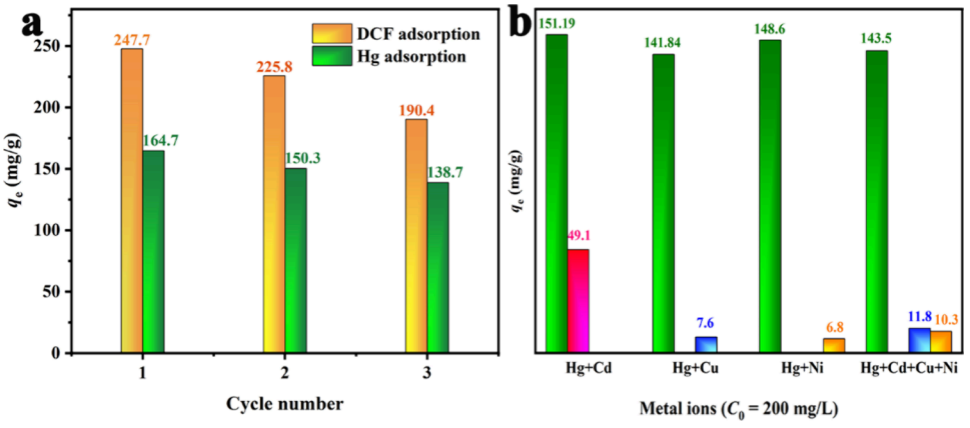

Figure 7. Regenerability (a) and selectivity (b) of GO-8/UiO-66-$(OH)_2$.

https://doi.org/10.1021/acsomega.4c09459
ACS Omega 2025, 10, 17269−17279

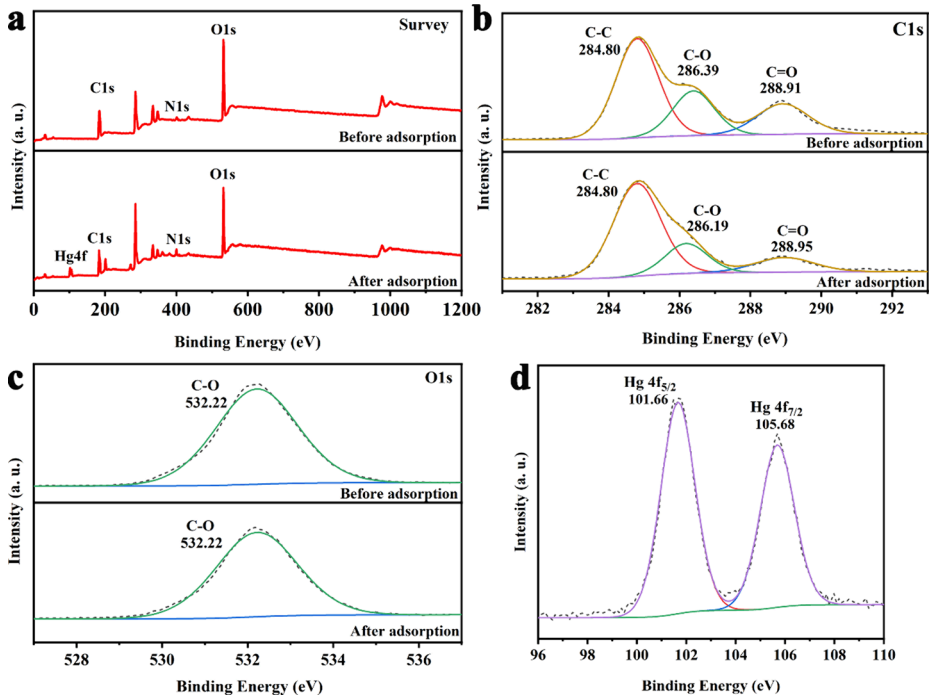

Figure 8. XPS spectra (a), C element (b), O element (c), and Hg element (d) of GO-8/UiO-66-$(OH)_2$ before and after adsorption.

easily reversible physisorption interactions, while Hg adsorption may involve stronger chemisorptive interactions, resulting in a more gradual decline in adsorption capacity over multiple cycles.

Moreover, great affinity of GO-8/UiO-66-$(OH)_2$ toward Hg^{2+} was demonstrated by the selectivity tests. The selectivity results for GO-8/UiO-66-$(OH)_2$ demonstrate its exceptionally high selectivity for Hg compared to other coexisting metal ions (Figure 7b). As shown, in the presence of competing ions such as Cd^{2+}, Cu^{2+}, and Ni^{2+}, the adsorption capacity for Hg remains significantly higher, with values such as 151.19 mg/g (Hg^{2+} + Cd^{2+}), 141.84 mg/g (Hg^{2+}+ Cu^{2+}), 148.6 mg/g (Hg^{2+} + Ni^{2+}), and 143.5 mg/g (Hg^{2+} + Cd^{2+} + Cu^{2+} + Ni^{2+}). In contrast, the adsorption capacities for the competing metal ions are considerably lower, ranging from 6.8 to 49.1 mg/g. This pronounced selectivity for Hg^{2+} suggests that GO-8/UiO-66-$(OH)_2$ possesses a strong affinity toward mercury ions, likely due to specific binding interactions between Hg^{2+} and the functional groups on the adsorbent surface, which favor Hg^{2+} adsorption over other metals even in competitive environments.

In the DCF and Hg^{2+} binary component system (the initial concentrations of DCF and Hg^{2+} were 300 and 100 mg/L), the coadsorption capacity of GO-8/UiO-66-$(OH)_2$ toward DCF and Hg^{2+} reached 195.8 and 144.1 mg/g. Due to the difference in the MW(molecular weight) of DCF and Hg^{2+}, it is more accurate to compare the adsorption capacity in terms of mmol/g instead of mg/g. The adsorption capacity of GO-8/UiO-66-$(OH)_2$ in the binary component system is 1.34 mmol/g, while in the single component system, it is 0.78 mmol/g and 0.82 mmol/g for DCF and Hg^{2+}, respectively, demonstrating great applicability of GO-8/UiO-66-$(OH)_2$ in the real multicomponent system.

3.2.7. Adsorption Mechanism. The XPS analysis conducted before and after the adsorption of DCF and Hg^{2+} onto GO-8/UiO-66-$(OH)_2$ elucidates critical aspects of the adsorption mechanisms and the specific interactions between the adsorbent and the two adsorbates. In the survey spectra (Figure 8a), the emergence of distinct Hg 4f peaks after adsorption indicates the successful binding of Hg^{2+} onto the surface of GO-8/UiO-66-$(OH)_2$. The consistent presence of C 1s, O 1s, and N 1s peaks before and after adsorption suggests that the structural integrity of the adsorbent remains intact throughout the adsorption process. The high-resolution C 1s spectra (Figure 8b) display minimal shifts in the binding energies of C−C (284.80 eV), C−O (286.19 eV), and C═O (288.95 eV) peaks following adsorption, indicating that the primary carbon backbone of the adsorbent does not undergo significant alteration.[44] This suggests that the adsorption of DCF and Hg^{2+} occurs predominantly at the surface through specific interactions rather than via changes in the adsorbent's structure. The O 1s spectra (Figure 8c) show the C−O peak remaining at 532.22 eV,[45] indicating the stability of oxygen-containing functional groups, which may facilitate surface complexation, particularly with Hg^{2+}.

The appearance of well-defined Hg 4f peaks at 101.66 and 105.68 eV, respectively,[46] in Figure 8d confirms the chemisorption of Hg^{2+} on the surface of GO-8/UiO-66-$(OH)_2$. This is likely driven by coordination between Hg^{2+} and oxygen-containing functional groups, such as hydroxyl or carboxyl groups, contributing to the high selectivity for Hg^{2+}. The chemisorption mechanism is consistent with the strong affinity observed for Hg^{2+}, suggesting the formation of stable surface complexes. In contrast, the lack of significant changes in the C 1s and O 1s spectra indicates that DCF adsorption likely occurs via weaker, noncovalent interactions, such as van der Waals forces or $\pi-\pi$ interactions, implying a physisorption-dominated mechanism.

Moreover, the XPS spectra of the Zr−O binding energy before and after the adsorption of Hg^{2+} onto the GO/UiO-66-$(OH)_2$ composite are measured and shown in Figure S2. The slight shift in the Zr−O binding energy after adsorption

https://doi.org/10.1021/acsomega.4c09459
ACS Omega 2025, 10, 17269−17279

indicates potential interactions between Hg^{2+} ions and the oxygen coordination site within the UiO-66-$(OH)_2$. This suggests that the Zr−O bond plays a role in stabilizing the adsorbed Hg^{2+} ions. The Zr 3d5/2 and Zr 3d3/2 peaks shift by ∼0.5 eV to higher binding energies (from 182.49 and 185.04 eV to 183.06 and 185.45 eV, respectively), reflecting changes in the local electronic environment of Zr atoms due to interactions with adsorbed Hg.[47−49] The peak intensities of Zr decreased after Hg adsorption. This reduction is attributed to the occupation of the adsorption sites.

The XPS results provide clear evidence that the adsorption of Hg onto GO-8/UiO-66-$(OH)_2$ is primarily governed by chemisorption, involving a strong coordination with oxygen functional groups. Meanwhile, DCF adsorption is predominantly physisorptive, involving weaker surface interactions. These findings explain the high selectivity and affinity of the adsorbent for Hg^{2+}, particularly in the presence of competing ions, and the less pronounced interactions with DCF.

4. CONCLUSIONS

This work synthesized a series of GO/UiO-66-$(OH)_2$ composites for the efficient uptake of DCF and Hg^{2+} in single- and binary-component systems. Structural and morphology characteristics of the composites are elucidated by XRD, FT-IR, and SEM. The addition of GO enhances the thermal stability and reduces the aggregation but maintains the great crystallinity of MOF particles. Batch adsorption tests are carried out to optimize the GO dosage, time, adsorbate concentration and temperature. The addition of GO increases the adsorption capacity by not only regulating the adsorbent morphology but also introducing additional adsorption sites, with the highest uptake amounts of DCF and Hg^{2+} reaching 324.2 and 429.3 mg/g on GO-8/UiO-66-$(OH)_2$, respectively. The weak affinity of GO-8/UiO-66-$(OH)_2$ toward Hg^{2+} compared to DCF is verified by the slower adsorption rate. Although pseudo-second-order, intraparticle diffusion models and the Freundlich isotherm are satisfactory for all the adsorption processes, different thermodynamic characters are observed in the adsorption process of DCF and Hg^{2+}, suggesting that DCF adsorption is primarily driven by physical interactions, while the adsorption of Hg^{2+} is endothermic and favored at higher temperatures. Moreover, the applicability of GO-8/UiO-66-$(OH)_2$ is demonstrated by the stable regeneration, high selectivity, and simultaneous adsorption processes. The XPS results provide clear evidence that the adsorption of Hg onto GO-8/UiO-66-$(OH)_2$ is primarily governed by chemisorption, involving strong coordination with oxygen functional groups. Meanwhile, DCF adsorption is predominantly physisorptive, involving weaker surface interactions. These findings explain the high selectivity and affinity of the adsorbent for Hg^{2+}, particularly in the presence of competing ions, and the less pronounced interactions with DCF.

■ ASSOCIATED CONTENT

Supporting Information

The Supporting Information is available free of charge at https://pubs.acs.org/doi/10.1021/acsomega.4c09459.

Characterization, selectivity test and binary-component adsorption test, the adsorption models (adsorption kinetics, isotherms and thermodynamics), the N_2 adsorption/desorption isotherm and pore size distribution, and the XPS spectra of Zr element of GO-8/UiO-66-$(OH)_2$ before and after adsorption (PDF)

■ AUTHOR INFORMATION

Corresponding Author

Shifeng Wang − *Key Laboratory of Plateau Oxygen and Living Environment of Tibet Autonomous Region, College of Science, Tibet University, Lhasa 850000, China;* orcid.org/0000-0001-6169-2598; Email: wsf365@163.com

Authors

Tao Shen − *Hoffmann Institute of Advanced Materials, Shenzhen Polytechnic University, Nanshan, Shenzhen 518055, China;* orcid.org/0009-0004-5526-959X

Guodong Wu − *Center of New Energy Research, School of Intelligence Science and Technology (School of Future Technology), Xinjiang University, Urumqi 830047, China*

Li Yin − *Hoffmann Institute of Advanced Materials, Shenzhen Polytechnic University, Nanshan, Shenzhen 518055, China*

Tianen Chen − *Center of New Energy Research, School of Intelligence Science and Technology (School of Future Technology), Xinjiang University, Urumqi 830047, China*

JiYe Fan − *Hebei Chemical & Pharmaceutical College, Shijiazhuang City, Hebei Province 050026, P.R. China*

Yuanhao Wang − *Hoffmann Institute of Advanced Materials, Shenzhen Polytechnic University, Nanshan, Shenzhen 518055, China*

Complete contact information is available at: https://pubs.acs.org/10.1021/acsomega.4c09459

Notes

The authors declare no competing financial interest.

■ ACKNOWLEDGMENTS

The research was supported by the Shenzhen Polytechnic University−Well Success Deuterium Depleted Water (DDW) R&D Center (602331014PQ). T.S. gratefully acknowledges the financial support from Postdoctoral Foundation Project of Shenzhen Polytechnic (6022331005K). L.Y. gratefully acknowledges the financial support from Postdoctoral Foundation Project of Shenzhen Polytechnic (6022331006K). This research is also supported by the Science Research Project of Hebei Education Department, ZD2021036.

■ REFERENCES

(1) Marghade, D.; Shelare, S.; Prakash, C.; Soudagar, M. E. M.; Khan, T. M. Y.; Kalam, M. A. Innovations in metal-organic frameworks (MOFs): Pioneering adsorption approaches for persistent organic pollutant (POP) removal. *Environ. Res.* **2024**, *258*, No. 119404.

(2) Rego, R. M.; Sriram, G.; Ajeya, K. V.; Jung, H. Y.; Kurkuri, M. D.; Kigga, M. Cerium based UiO-66 MOF as a multipollutant adsorbent for universal water purification. *J. Hazard. Mater.* **2021**, *416*, No. 125941.

(3) Diab, K. E.; Salama, E.; Hassan, H. S.; Abd El-moneim, A.; Elkady, M. F. Biocompatible MIP-202 Zr-MOF tunable sorbent for cost-effective decontamination of anionic and cationic pollutants from waste solutions. *Sci. Rep.* **2021**, *11*, 6619.

(4) Wang, R. D.; Wei, W. M.; Li, H. Y.; Shen, T. Z.; Wang, L.; Zhou, S. H.; Zhang, W. Q.; Du, L.; Zhao, Q. H. Metal-Organic framework derived vulcanized functional materials for ultra-efficient treatment of Hg(II) ions in water. *J. Mol. Liq.* **2024**, *401*, No. 124609.

(5) Hasan, Z.; Khan, N.; Jhung, S. Adsorptive removal of diclofenac sodium from water with Zr-based metal−organic frameworks. *Chemical Engineering Journal* **2016**, *284*, 1406−1413.
(6) Bhadra, B.; Seo, P.; Jhung, S. Adsorption of diclofenac sodium from water using oxidized activated carbon. *Chemical Engineering Journal* **2016**, *301*, 27−34.
(7) Miretzky, P.; Cirelli, A. Hg(II) removal from water by chitosan and chitosan derivatives: A review. *Journal of Hazardous Materials* **2009**, *167*, 10−23.
(8) Shirzadi, H.; Nezamzadeh-Ejhieh, A. An efficient modified zeolite for simultaneous removal of Pb(II) and Hg(II) from aqueous solution. *J. Mol. Liq.* **2017**, *230*, 221−229.
(9) Jiang, J.; Shi, Y.; Wu, M.; Rezakazemi, M.; Aminabhavi, T. M.; Huang, R.; Jia, C.; Ge, S. Biomass-MOF composites in wastewater treatment, air purification, and electromagnetic radiation adsorption - A review. *Chemical Engineering Journal* **2024**, *494*, No. 152932.
(10) Jeong, C.; Ansari, M. Z.; Hakeem Anwer, A.; Kim, S. H.; Nasar, A.; Shoeb, M.; Mashkoor, F. A review on metal-organic frameworks for the removal of hazardous environmental contaminants. *Sep. Purif. Technol.* **2023**, *305*, No. 122416.
(11) Yu, F.; Bai, X. T.; Liang, M. X.; Ma, J. Recent progress on metal-organic framework-derived porous carbon and its composite for pollutant adsorption from liquid phase. *Chemical Engineering Journal* **2021**, *405*, No. 126960.
(12) Feng, Y. H.; Su, X. W.; Chen, Y.; Liu, Y. Y.; Zhao, X. A.; Lu, C. G.; Ma, Y.; Lu, G. X.; Ma, M. L. Research progress of graphene oxide-based magnetic composites in adsorption and photocatalytic degradation of pollutants: A review. *Mater. Res. Bull.* **2023**, *162*, No. 112207.
(13) Wang, S. F.; Li, X.; Liu, Y. G.; Zhang, C.; Tan, X. F.; Zeng, G. M.; Song, B. A.; Jiang, L. H. Nitrogen-containing amino compounds functionalized graphene oxide: Synthesis, characterization and application for the removal of pollutants from wastewater: A review. *Journal of Hazardous Materials* **2018**, *342*, 177−191.
(14) Sun, Y. Z.; Chen, M.; Liu, H.; Zhu, Y.; Wang, D. B.; Yan, M. Adsorptive removal of dye and antibiotic from water with functionalized zirconium-based metal organic framework and graphene oxide composite nanomaterial Uio-66-$(OH)_2$/GO. *Appl. Surf. Sci.* **2020**, *525*, No. 146614.
(15) Mukherjee, D.; Das, P.; Prasad, G. N.; Katha, A. R.; Gumma, S.; Mandal, B. Hierarchical graphite oxide decorated UiO-66 for ultrahigh adsorption of dye with synergistic effect of ultrasonication: Experimental and density functional theory study. *Sep. Purif. Technol.* **2022**, *294*, No. 121217.
(16) Li, Y. H.; Liu, M. Y.; Wei, Y. W.; Wang, C. C.; Wang, P. Adsorption and photocatalytic desorption toward Cr(vi) over defect-induced hierarchically porous UiO-66-$(OH)_2$: a sustainable approach. *Environmental Science: Nano* **2023**, *10*, 672−682.
(17) Chen, J. H.; Xing, H. T.; Guo, H. X.; Weng, W.; Hu, S. R.; Li, S. X.; Huang, Y. H.; Sun, X.; Su, Z. B. Investigation on the adsorption properties of Cr(VI) ions on a novel graphene oxide (GO) based composite adsorbent. *J. Mater. Chem. A* **2024**, *2*, 12561−12570.
(18) Wu, S. C.; Yu, L. L.; Xiao, F. F.; You, X.; Yang, C.; Cheng, J. H. Synthesis of aluminum-based MOF/graphite oxide composite and enhanced removal of methyl orange. *J. Alloys Compd.* **2017**, *724*, 625−632.
(19) Rada, Z. H.; Abid, H. R.; Shang, J.; Sun, H.; He, Y. D.; Webley, P.; Liu, S. M.; Wang, S. B. Functionalized UiO-66 by Single and Binary $(OH)_2$ and NO_2 Groups for Uptake of CO_2 and CH_4. *Ind. Eng. Chem. Res.* **2016**, *55*, 7924−7932.
(20) Rada, Z. H.; Abid, H. R.; Sun, H.; Wang, S. Bifunctionalized Metal Organic Frameworks, UiO-66-NO_2-N (N = -NH_2, -$(OH)_2$, -$(COOH)_2$), for Enhanced Adsorption and Selectivity of CO_2 and N_2. *Journal of Chemical & Engineering Data* **2015**, *60*, 2152−2161.
(21) Vo, T. K.; Nguyen, V. C.; Quang, D. T.; Park, B.; Kim, J. Formation of structural defects within UiO-66(Zr)-$(OH)_2$ framework for enhanced CO_2 adsorption using a microwave-assisted continuous-flow tubular reactor. *Microporous Mesoporous Mater.* **2021**, *312*, No. 110746.
(22) Hu, Z.; Kang, Z.; Qian, Y.; Peng, Y.; Wang, X.; Chi, C.; Zhao, D. Mixed Matrix Membranes Containing UiO-66(Hf)-$(OH)_2$ Metal−Organic Framework Nanoparticles for Efficient H_2/CO_2 Separation. *Ind. Eng. Chem. Res.* **2016**, *55*, 7933−7940.
(23) Yang, S.; Gao, M.; Luo, Z.; Yang, Q. The characterization of organo-montmorillonite modified with a novel aromatic-containing gemini surfactant and its comparative adsorption for 2-naphthol and phenol. *Chemical Engineering Journal* **2015**, *268*, 125−134.
(24) Xue, G.; Gao, M.; Gu, Z.; Luo, Z.; Hu, Z. The removal of p-nitrophenol from aqueous solutions by adsorption using gemini surfactants modified montmorillonites. *Chemical Engineering Journal* **2013**, *218*, 223−231.
(25) Liu, Y.; Gan, D.; Chen, M.; Ma, L.; Yang, B.; Li, L.; Zhu, M.; Tu, W. Bioinspired dopamine modulating graphene oxide nanocomposite membrane interposed by super-hydrophilic UiO-66 with enhanced water permeability. *Sep. Purif. Technol.* **2020**, *253*, No. 117552.
(26) Jayaramulu, K.; Mukherjee, S.; Morales, D.; Dubal, D.; Nanjundan, A.; Schneemann, A.; Masa, J.; Kment, S.; Schuhmann, W.; Otyepka, M.; Zboril, R.; Fischer, R. Graphene-Based Metal−Organic Framework Hybrids for Applications in Catalysis, Environmental, and Energy Technologies. *Chem. Rev.* **2022**, *122*, 17241−17338.
(27) Li, Z.; Gómez-Avilés, A.; Sellaoui, L.; Bedia, J.; Bonilla-Petriciolet, A.; Belver, C. Adsorption of ibuprofen on organo-sepiolite and on zeolite/sepiolite heterostructure: Synthesis, characterization and statistical physics modeling. *Chemical Engineering Journal* **2019**, *371*, 868−875.
(28) Wang, J.; Gao, M.; Shen, T.; Yu, M.; Xiang, Y.; Liu, J. Insights into the efficient adsorption of rhodamine B on tunable organo-vermiculites. *Journal of Hazardous Materials* **2019**, *366*, 501−511.
(29) Qiu, H.; Lv, L.; Pan, B. C.; Zhang, Q. J.; Zhang, W. M.; Zhang, Q. X. Critical review in adsorption kinetic models. *J. Zhejiang Univ., Sci., A* **2009**, *10*, 716−724.
(30) Wang, J.; Guo, X. Adsorption kinetic models: Physical meanings, applications, and solving methods. *Journal of Hazardous materials* **2020**, *390*, No. 122156.
(31) Musah, M.; Azeh, Y.; Mathew, J. T.; Umar, M. T.; Abdulhamid, Z.; Muhammad, A. I. Adsorption kinetics and isotherm models: a review. *CaJoST* **2022**, *4*, 20−26.
(32) Al-Ghouti, M. A.; Da'ana, D. A. Guidelines for the use and interpretation of adsorption isotherm models: A review. *J. Hazard. Mater.* **2020**, *393*, No. 122383.
(33) Foo, K. Y.; Hameed, B. H. Insights into the modeling of adsorption isotherm systems. *Chemical Engineering Journal* **2010**, *156*, 2−10.
(34) Wang, J.; Guo, X. Adsorption isotherm models: Classification, physical meaning, application and solving method. *Chemosphere* **2020**, *258*, No. 127279.
(35) Bulut, Y.; Aydin, H. A kinetics and thermodynamics study of methylene blue adsorption on wheat shells. *Desalination* **2006**, *194*, 259−267.
(36) Albadarin, A.; Mangwandi, C.; Al-Muhtaseb, A.; Walker, G.; Allen, S.; Ahmad, M. Kinetic and thermodynamics of chromium ions adsorption onto low-cost dolomite adsorbent. *Chemical Engineering Journal* **2012**, *179*, 193−202.
(37) Marczewski, A.; Seczkowska, M.; Derylo-Marczewska, A.; Blachnio, M. Adsorption equilibrium and kinetics of selected phenoxyacid pesticides on activated carbon: effect of temperature. *Adsorption* **2016**, *22*, 777−790.
(38) Doke, K. M.; Khan, E. M. Adsorption thermodynamics to clean up wastewater; critical review. *Reviews in Environmental Science and Bio/Technology* **2013**, *12*, 25−44.
(39) Al-Anber, M. A.Thermodynamics approach in the adsorption of heavy metals. In *Thermodynamics-Interaction Studies-Solids, Liquids and Gases*; IntechOpen: 2011.
(40) Zhao, Y.; Liu, F.; Qin, X. Adsorption of diclofenac onto goethite: Adsorption kinetics and effects of pH. *Chemosphere* **2017**, *180*, 373−378.

https://doi.org/10.1021/acsomega.4c09459
ACS Omega 2025, 10, 17269−17279

(41) Nam, S.; Jung, C.; Li, H.; Yu, M.; Flora, J.; Boateng, L.; Her, N.; Zoh, K.; Yoon, Y. Adsorption characteristics of diclofenac and sulfamethoxazole to graphene oxide in aqueous solution. *Chemosphere* **2015**, *136*, 20−26.
(42) Zuo, S.; Sun, Y.; Zheng, Y.; Sun, X.; Hu, J. Efficient selective uptake of Hg(II) using a porous organic polymer rich in N and S atoms. *Journal of Environmental Chemical Engineering* **2024**, *12*, No. 111924.
(43) Nouri, M.; Hajiaghababaei, L.; Badiei, A.; Khalilian, F.; Mazloomifar, A. Dual-functional ratiometric fluorescence sensor based on silica spheres for highly selective detection of Hg^{2+} and Fe^{3+}. *Colloids Surf., A* **2025**, *706*, No. 135755.
(44) Liu, H.; Zhang, X.; Hou, L.; Zheng, H.; Niu, B.; Weng, K.; Liu, S.; Fu, J. Nitrogen-rich hierarchical porous polyphosphazene for rapid and efficient adsorption of anionic contaminants: Kinetics, isotherm, thermodynamics and mechanism. *Appl. Surf. Sci.* **2023**, *616*, No. 156538.
(45) Wei, H.; Li, S.; Bao, J.; Jalil Shah, S.; Luan, X.; He, C.; Zhao, Z.; Zhao, Z. Construction of dual-imprinted UiO-66 s for highly efficient and synergistic Co-adsorption of diclofenac sodium and Cu (II). *Sep. Purif. Technol.* **2022**, *300*, No. 121901.
(46) Guo, Z.; Li, N.; Zuo, S.; Qiang, C.; Zhan, W.; Li, Z.; Ma, J. Ma, onstruction of a novel metal−organic framework adenine-UiO-66 piezocatalyst for efficient diclofenac removal. *Sep. Purif. Technol.* **2022**, *289*, No. 120743.
(47) Chen, C.; Chen, D.; Xie, S.; Quan, H.; Luo, X.; Guo, L. Adsorption Behaviors of Organic Micropollutants on Zirconium Metal−Organic Framework UiO-66: Analysis of Surface Interactions. *ACS Appl. Mater. Interfaces* **2017**, *9*, 41043−41054.
(48) Wang, A.; Zhou, Y.; Wang, Z.; Chen, M.; Sun, L.; Liu, X. Titanium incorporated with UiO-66(Zr)-type Metal−Organic Framework (MOF) for photocatalytic application. *RSC Adv.* **2016**, *6*, 3671−3679.
(49) Guan, T.; Li, X.; Fang, W.; Wu, D. Efficient removal of phosphate from acidified urine using UiO-66 metal-organic frameworks with varying functional groups. *Appl. Surf. Sci.* **2020**, *501*, No. 144074.

https://doi.org/10.1021/acsomega.4c09459
ACS Omega 2025, 10, 17269−17279